Nanoscale

2D/2D Heterojunction of Ti3C2/g-C3N4 Nanosheets for Enhanced Photocatalytic Hydrogen Evolution

Journal:	*Nanoscale*
Manuscript ID	NR-ART-01-2019-000168.R1
Article Type:	Paper
Date Submitted by the Author:	30-Jan-2019

Complete List of Authors:	Su, Tongming; Guangxi University, Hood, Zachary; Massachusetts Institute of Technology Naguib, Michael; Tulane University Bai, Lei; Oak Ridge National Laboratory Luo, Si; Oak Ridge National Laboratory Rouleau, Christopher; Oak Ridge National Laboratory, Material Science and Technology Ivanov, Ilia; Oak Ridge National Laboratory, Center for Nanophase Materials Science Ji, Hongbing; Sun Yat-sen University, School of Chemistry Qin, Zu-Zeng; Guangxi Univeristy, School of Chemistry and Chemical Engineering Wu, Zili; Oak Ridge National Laboratory, Chemical Science Division and Center for Nanophase Materials Sciences

Nanoscale

ARTICLE

2D/2D Heterojunction of Ti_3C_2/g-C_3N_4 Nanosheets for Enhanced Photocatalytic Hydrogen Evolution

Tongming Su,*[a,b] Zachary D. Hood,[b,d] Michael Naguib,[c] Lei Bai,[b,f] Si Luo,[b] Christopher M. Rouleau,[b] Ilia N. Ivanov,[b] Hongbing Ji,[a,e] Zuzeng Qin,*[a] and Zili Wu*[b]

Photocatalytic hydrogen evolution from water has received enormous attention due to its ability to address a number of global environmental and energy-related issues. Here, we synthesize 2D/2D Ti_3C_2/g-C_3N_4 composites by electrostatic self-assembly and demonstrate their use as catalysts for hydrogen evolution under visible light irradiation. The optimized Ti_3C_2/g-C_3N_4 composites exhibited a 10 times higher photocatalytic hydrogen evolution performance (72.3 μmol h^{-1} g_{cat}^{-1}) than that of pristine g-C_3N_4 (7.1 μmol h^{-1} g_{cat}^{-1}). Such enhanced photocatalytic performance was due to the formation of 2D/2D heterojunctions in the Ti_3C_2/g-C_3N_4 composites. The intimate contact between the monolayer Ti_3C_2 and g-C_3N_4 nanosheets promotes the separation of photogenerated charge carriers at the Ti_3C_2/g-C_3N_4 interface. Furthermore, the ultrahigh conductivity of Ti_3C_2 and the Schottky junction formed between g-C_3N_4-MXene interfaces facilitate the photoinduced electron transfer and suppress the recombination with photogenerated holes. This work demonstrates that the 2D/2D Ti_3C_2/g-C_3N_4 composites are promising photocatalysts thanks to the ultrathin MXenes as efficient co-catalysts for photocatalytic hydrogen production.

Received 00th January 20xx,
Accepted 00th January 20xx

DOI: 10.1039/x0xx00000x

www.rsc.org/

Introduction

With the development of human society and the increasing consumption of fossil fuels, renewable chemical fuels have attracted intensive research attention over the past decades.[1] Converting solar energy into chemical energy in the form of hydrogen is an ideal route to obtain clean renewable energy resources.[2, 3] Due to the fact that water and solar energy are inexhaustible, photocatalytic water splitting into hydrogen over a semiconductor with visible light represents a promising strategy to store solar energy as chemical energy. The key of photocatalytic water splitting lies in the development of cheap and highly-active photocatalysts that function under visible light irradiation. Over the past decades, various semiconductors, such as metal oxides,[4] sulphides,[5, 6] metal oxynitrides,[7] nitrides,[8] amongst others, have been used as photocatalysts for hydrogen evolution. Among these photocatalysts, graphitic carbon nitride (g-C_3N_4) grabs considerable attention in the field of visible-light photocatalytic water splitting due to its suitable band structure, high thermal and chemical stability, low cost, non-toxicity, and high surface area.[9, 10]

Unfortunately, the rapid recombination of photogenerated electrons and holes on g-C_3N_4 largely hinders its practical application in photocatalytic water splitting.[9] Various strategies have been developed to improve the separation of photoinduced electron-hole pairs on g-C_3N_4, such as structural engineering,[11] increasing the crystallinity,[12, 13] doping with heteroatom,[14] construction of heterojunction,[15-18] and coupling with a co-catalyst.[19, 20] Among these approaches, co-catalyst loading is an effective method to promote the separation of photoinduced electron-hole pairs. For example, Pt, MoS_2, and graphene can all be used as co-catalysts to capture the photo-induced electrons, thus inhibited the recombination of photoinduced charge carriers.[21, 22] Among them, Pt is the most efficient co-catalyst for photocatalytic hydrogen evolution. However, the high cost and scarcity of this noble metal limit its large-scale application. Therefore, the development of low-cost and effective co-catalysts is imperative to meet the requirements of industrial applications of semiconductor-based photocatalysts.

MXenes, a new family of two-dimensional (2D) materials of early transition metal carbides/carbonitrides, has attracted a great deal of research interest since it was discovered by Gogotsi and coworkers in 2011.[23] Attributing to its excellent electrical conductivity, hydrophilicity, and stability, MXenes have been extensively investigated for various applications, such as electrochemical supercapacitors,[24] batteries,[25] biomedicine,[26] catalysis,[27] among other

[a] School of Chemistry and Chemical Engineering, Guangxi University, Nanning 530004, China. E-mail: sutm@gxu.edu.cn, qinzuzeng@gxu.edu.cn
[b] Center for Nanophase Materials Sciences, Oak Ridge National Laboratory, Oak Ridge, Tennessee 37831, USA. E-mail: wuz1@ornl.gov
[c] Department of Physics and Engineering Physics, Tulane University, New Orleans, Louisiana 70118, USA.
[d] Electrochemical Materials Laboratory, Department of Materials Science and Engineering, Massachusetts Institute of Technology, Cambridge, Massachusetts 02139, USA.
[e] School of Chemistry, Sun Yat-sen University, Guangzhou 510275, China.
[f] West Virginia University, Department of Chemical and Biomedical Engineering, Morgantown, West Virginia 26506, USA.

†Electronic Supplementary Information (ESI) available: Supplemental characterization of photocatalysts by XRD, Raman, SEM, AFM, BET, EDS, XPS, UV-vis absorption, and PL, additional photocatalytic experiments, characterization of used photocatalysts by XRD, UV-vis absorption, BET, SEM, and XPS. See DOI: 10.1039/x0xx00000x

applications. The theoretical studies show that the Gibbs free energy for hydrogen adsorption (ΔG_H) of several MXenes are close to zero, thus these MXenes are considered as effective electrocatalysts for the hydrogen evolution reaction.[28, 29] Furthermore, the electrocatalytic hydrogen evolution activity of MXenes was confirmed by experiment.[30] With the near-zero ΔG_H, electrical conductivity, hydrophilicity, and low Fermi level compared to semiconductors, MXene may be an effective co-catalyst for photocatalytic hydrogen production from water. Recently, MXenes, such as Ti_3C_2, Ti_2C, and Nb_2C have been investigated as efficient co-catalysts of photocatalysts (*e.g.* TiO_2, CdS, g-C_3N_4) for water splitting.[31-35] When MXene was coupled with semiconductors, a Schottky barrier will be presented at the MXene/semiconductor interface.[33] The Schottky barrier can serve as the electron reservoir, thus facilitating the separation of photoinduced electrons and holes. For example, the Ti_3C_2 nanoparticles (0D) can be used as the co-catalyst to enhance the photocatalytic hydrogen production of g-C_3N_4.[34] Nevertheless, the Ti_3C_2/g-C_3N_4 shows a 0D/2D type heterojunction, and this 0D/2D heterojunction possesses a limited interface between the Ti_3C_2 and g-C_3N_4. Furthermore, due to the multilayer nature of Ti_3C_2, the photogenerated electrons have to transfer a long distance to the surface of the catalyst, which lead to the poor separation of charge carriers. Therefore, an intimate interfacial contact between Ti_3C_2 and g-C_3N_4 is needed in order to improve charge separation efficiency.

Construction of 2D/2D heterojunction, with obvious advantages over the 0D/2D heterojunction, is considered as an effective route to enhance the charge separation efficiency and improve the photocatalytic hydrogen evolution.[2] Firstly, the 2D/2D heterojunction has much more contact areas than that of 0D/2D. Secondly, the intimate 2D/2D heterojunction improves the electron transfer rate and shortens the migration distance and time of photogenerated electrons to the catalyst surface. Therefore, the photocatalytic hydrogen production can be greatly enhanced through the formation of a 2D/2D heterojunction. For example, the photocatalytic hydrogen production rate over 2D/2D g-C_3N_4/$ZnIn_2S_4$ is 8.2 times higher than that of 0D/2D g-C_3N_4/$ZnIn_2S_4$.[36] Recently, d-Ti_3C_2/TiO_2/g-C_3N_4 heterostructured composite was synthesized and used for photocatalytic hydrogen production. In this system, delaminated Ti_3C_2 (d-Ti_3C_2) served as the fast electron transfer channel to develop the separation efficiency of the photogenerated charge carriers, thus enhance the photocatalytic activity of g-C_3N_4. However, this d-Ti_3C_2 still exhibit multilayered structure, and the hydrogen evolution rate of the optimal d-Ti_3C_2/TiO_2/g-C_3N_4 composites showed only 2.4 times higher than that of the pure g-C_3N_4 with 3.0 wt% Pt as the co-catalyst.[37] To shed more light on the effect of the 2D MXene and the 2D/2D heterojunction on the photocatalytic activity of the photocatalyst, in this work, monolayer Ti_3C_2 and g-C_3N_4 nanosheets were successfully prepared and the 2D/2D Ti_3C_2/g-C_3N_4 composites were synthesized by electrostatic self-assembly technique. The hydrogen evolution rate of obtained 2D/2D Ti_3C_2/g-C_3N_4 nanosheets showed over 10 times higher than that of the pure g-C_3N_4, and also significantly higher than that of the 0D/2D Ti_3C_2/g-C_3N_4, and the 2D/2D graphene/g-C_3N_4 without any noble metal as the co-catalyst. Such enhanced activity is largely attributed to the intimate interfacial contact between the monolayer Ti_3C_2 and g-C_3N_4 nanosheets and the highly active sites on the monolayer Ti_3C_2.

Experimental section

Synthesis of bulk g-C_3N_4 and g-C_3N_4 nanosheets

Bulk g-C_3N_4 powder was synthesized by thermal polymerization of urea. Briefly, urea (25 g) was placed into a covered ceramic crucible, and then the crucible was heated to 600 °C at a ramp rate of 5 °C min^{-1} and maintained for 4 h. After cooling to room temperature, the resulting light-yellow solid was ground with the mortar to obtain the bulk g-C_3N_4 powder (denoted as B-g-C_3N_4). To obtain the g-C_3N_4 nanosheet, B-g-C_3N_4 (1.0 g) was placed in an open ceramic crucible and was heated to 550 °C with a ramp rate of 5 °C min^{-1} and held in an ambient air atmosphere for 2 h. Finally, a light yellow powder of g-C_3N_4 nanosheets was obtained, which is herein denoted as g-C_3N_4.

Synthesis of multilayer Ti_3C_2 and monolayer Ti_3C_2

The Ti_3AlC_2 was prepared according to the previous reports.[23] Briefly, commercial Ti_2AlC and TiC were mixed evenly and heated to 1350 ºC for 2 h under continuous flow of argon gas, Ar, to obtain Ti_3AlC_2. To synthesize the multilayer Ti_3C_2 (M-Ti_3C_2), Ti_3AlC_2 powder (2.0 g) was immersed into of a 48% HF aqueous solution (20 mL) and stirred at room temperature for 15 h. The obtained Ti_3C_2 suspension was washed with deionized (DI) water several times and centrifuged to separate the multilayer Ti_3C_2 from the solution. After that, the multilayer Ti_3C_2 was dried with a vacuum oven. Monolayer Ti_3C_2 was prepared via a previously reported method.[38] In short, LiF (1.0 g) was dissolved completely in 6 M HCl (20 mL) under stirring at room temperature to obtain the LiF/HCl solution. Then, Ti_3AlC_2 (1.0 g) was slowly added to the obtained LiF/HCl solution over the course of 5 minutes. The temperature of the suspension was raised to 35 °C and maintained at this temperature for 24 h with vigorous stirring. The resulting suspension was washed with DI water repeatedly until the pH of the filtrate was $\geqslant$ 6. After that, the suspension was centrifuged at 8000 rpm to separate the un-delaminated Ti_3AlC_2 and the multilayer Ti_3C_2 from the monolayer Ti_3C_2 colloidal solution. The Ti_3C_2 colloidal solution was subsequently filtered through a PVDF membrane (0.25 μm pore size, Millipore) and dried in a vacuum oven at room temperature for 24 h to obtain the stacked monolayer of Ti_3C_2 (S-Ti_3C_2).

Synthesis of 2D/2D Ti_3C_2/g-C_3N_4

The 2D/2D Ti_3C_2/g-C_3N_4 was synthesized via electrostatic self-assembly approach. Firstly, g-C_3N_4 (0.3 g) was added to a 0.5 M HCl aqueous solution (100 mL) and protonated at room temperature for 0.5 h via sonication. After that, the protonated g-C_3N_4 was repeatedly washed with DI water until the pH of the g-C_3N_4 suspension was equal to 4. Secondly, 80 mg S-Ti_3C_2 was re-dispersed in 40 mL deionized water by sonication for 1 h in Ar atmosphere to obtain the 2 mg mL^{-1} monolayer Ti_3C_2 solution. After that, a quantitative monolayer Ti_3C_2 solution (1.0, 2.0, 3.0, 4.0, and 5.0 wt.%) was added dropwise to the above protonated g-C_3N_4 suspension and was stirred for 0.5 h. Then the suspension was centrifuged to obtain the Ti_3C_2/g-C_3N_4 precipitate, which was dried at 80 °C for 24 h. The Ti_3C_2/g-C_3N_4 composites with different amount of monolayer Ti_3C_2 (1.0, 2.0, 3.0, 4.0, and 5.0 wt.%) were denoted as 1-TC/CN, 2-TC/CN, 3-TC/CN, 4-TC/CN, and 5-TC/CN. The protonated g-C_3N_4 (P-g-C_3N_4) powder was obtained by the same method without adding Ti_3C_2. We applied the same approach by replacing monolayer Ti_3C_2 with multilayer Ti_3C_2 or graphene in

order to synthesize 3.0 wt.% M-Ti_3C_2/g-C_3N_4 (3-MTC/CN) and 3.0 wt.% graphene/g-C_3N_4 (3-G/CN), respectively. We also replaced g-C_3N_4 with B-g-C_3N_4 in order to prepare 3.0 wt.% Ti_3C_2/B-g-C_3N_4 (3-TC/BCN).

Photocatalytic hydrogen evolution reaction

Photocatalytic experiments were carried out in a side-irradiation quartz reactor. For comparison, the photocatalytic activity of the g-C_3N_4 by using 3.0 wt% Pt as the co-catalyst was investigated. The loading of 3.0 wt% Pt co-catalyst was conducted by directly dissolving H_2PtCl_6 into the suspension. Thereafter, the suspension was stirred and irradiated (200 W Hg lamp) for 30 min at room temperature to reduce the Pt species. For each experiment, the photocatalyst (30 mg) were dispersed in deionized water (40 mL) with 10% triethanolamine as the hole scavenger. Prior to the photocatalytic reaction, the system was degassed with ultrahigh pure argon for 30 min. The light input is provided by a 200 W Hg lamp equipped with a cutoff filter to allow the pass of light with wavelength higher than 400 nm. The solution was vigorously stirred during the photocatalytic reaction and the temperature was maintained at 25 °C by the circulating cooling water. The gas product was quantified by a gas chromatography (Model BUCK 910) equipped with a molecular sieve column and thermal conductivity detector (TCD) and with argon as the carrier gas.

Characterizations

X-ray diffraction (XRD) measurements were performed on a PANalytical X'Pert MPD Pro powder diffractometer equipped with a Si-based position-sensitive one-dimensional detector and Ni-filtered Cu Kα radiation source, and the X-rays were generated at 45 kV/40 mA at a beam wavelength of λ = 1.5416 Å (Cu Kα radiation). A Zeiss Merlin scanning electron microscope with an acceleration voltage of 20.0 kV was used for scanning electron microscope (SEM) imaging. High-resolution transmission electron microscopy (HRTEM) imaging of the samples was performed on an aberration-corrected FEI Titan S 80-300 STEM/TEM microscope equipped with a Gatan OneView camera at an acceleration voltage of 300 kV. The BET surface area of the samples was measured with a Quantachrome system using N_2 as the probe gas. An Acton Trivista 555 spectrometer (Princeton Instruments) with laser excitation at 325 nm was used to collect the Raman spectra. The UV–vis absorption spectra were recorded using a Cary 5000 UV/Vis spectrophotometer. Photoluminescence (PL) spectra were performed on a Horiba Jobin Yvon Fluorolog fluorescence spectrometer, and the excitation monochromator was set at 325 nm. X-ray photoelectron spectroscopy (XPS) was performed on a Thermo Scientific K-Alpha spectrometer at an operating pressure under 3.0×10^{-7} Pa and a spot size of 400 μm using an Al-Kα microfused monochromatized source (1486.6 eV) with a resolution of 0.1 eV. All XPS data was processed using Avantage Data System, which is a software package provided by Thermo Scientific. Atomic force microscopy (AFM) was performed on a Dimension Icon scanning probe microscope with the contact and tapping modes.

Photoelectrochemical measurements

Photoelectrochemical (PEC) measurements were performed on a BioLogic SP150 electrochemical workstation using a standard three-electrode cell with a working electrode, Ag/AgCl electrode as reference electrode and Pt mesh as the counter electrode. A 0.2 M Na_2SO_4 aqueous solution was utilized as the buffer solution. Electrochemical impedance spectroscopy (EIS) was collected in a range from 0.1 kHz to 100 kHz with an AC amplitude of 5 mV. The transient photocurrent was performed in the same three-electrode system, and the light source was a 200 W Hg lamp equipped with a cutoff filter (400 nm). The working electrodes were prepared as follows: 4 mg of the synthesized photocatalyst was first ultrasonically dispersed in the mixture of 250 μL of deionized water, 250 μL of ethanol and 20 μL of Nafion® solutions (Sigma Aldrich, 5 wt% in mixture of lower aliphatic alcohols and water, contains 45% water) for 1.0 h. After that, 20 μL of the catalyst suspension was transferred onto the indium tin oxide (ITO) substrate and dried at room temperature to obtain the working electrode.

Results and Discussion

The crystal structure of as-synthesized samples was studied by XRD analysis (Figure S1A and B, Supporting Information). As shown in Figure S1A, the XRD patterns of original Ti_3AlC_2 exhibit intense peaks, which is in accordance with the previous reports.[23] After reacting the MAX phase with a LiF/HCl solution, the most intense diffraction peak ($2\theta = 39°$) of Ti_3AlC_2 disappears in the XRD patterns for stacked monolayer of Ti_3C_2 (S-Ti_3C_2) (see Figure S2 for the photograph and SEM images of the cross-section of S-Ti_3C_2). Moreover, the (002) peak of Ti_3C_2 shifts to a lower angle due to the increased interlayer spacing of the Ti_3C_2, indicating the Ti_3AlC_2 was successfully transformed to Ti_3C_2. The XRD patterns of the g-C_3N_4 show two evident peaks (Figure S1A); the peak at 2θ = 13.3° is attributed to the in-plane structural packing motif, and the peak at 2θ = 27.7° is assigned to the interlayer stacking of aromatic segments.[39] The XRD patterns of the protonated g-C_3N_4 (P-g-C_3N_4) show similar diffraction peaks to that of g-C_3N_4, indicating that the protonation did not change the crystal structure of the g-C_3N_4. The Ti_3C_2/g-C_3N_4 composites were fabricated via an electrostatic self-assembly strategy. According to the previous reports, the surface of g-C_3N_4 nanosheet is positively charged after the protonation treatment,[40] while the surface of monolayer Ti_3C_2 is negatively charged.[41] Therefore, when the g-C_3N_4 suspension was mixed with the Ti_3C_2 colloidal solution, g-C_3N_4 and Ti_3C_2 will first stick together via electrostatic interaction and then coagulate at the bottom of the beaker (Figure S3, Supporting Information). The XRD patterns of the Ti_3C_2/g-C_3N_4 composites show similar diffraction peaks to that of g-C_3N_4, and no diffraction peaks of Ti_3C_2 was observed due to its low content and high dispersion (Figure S1B).

The chemical structure of the as-prepared samples was investigated by Raman spectroscopy (Figure S1C and D, Supporting Information). For the Raman spectra of the g-C_3N_4 and the Ti_3C_2/g-C_3N_4 composites, several characteristics peaks located at 480, 708, 771, 987, 1122, 1494, and 1629 cm^{-1} can be observed, confirming the formation of the polymeric structure of g-C_3N_4.[42, 43] In detail, two wide peaks located at 1355 cm^{-1} and 1587 cm^{-1} are assigned to the disordered sp^3 carbon (D band) and graphitic sp^2 carbon (G band) of a typical graphitic structure in the g-C_3N_4.[44] The Raman shifts at 500~1300 cm^{-1} originate from the typical heptazine units. The two peaks at 708 cm^{-1} and 771 cm^{-1} correspond to the in-plane bending

vibrations of the heptazine linkages, while the peaks at 987 cm^{-1} belonged to the symmetric N-breathing mode of heptazine units.[36] The Raman spectra of all the samples are notably similar, suggesting that the protonation, thermal exfoliation, and loading processes during the preparation of Ti_3C_2/g-C_3N_4 composites did not change the chemical structure of the g-C_3N_4. In addition, no Raman peaks of Ti_3C_2 can be

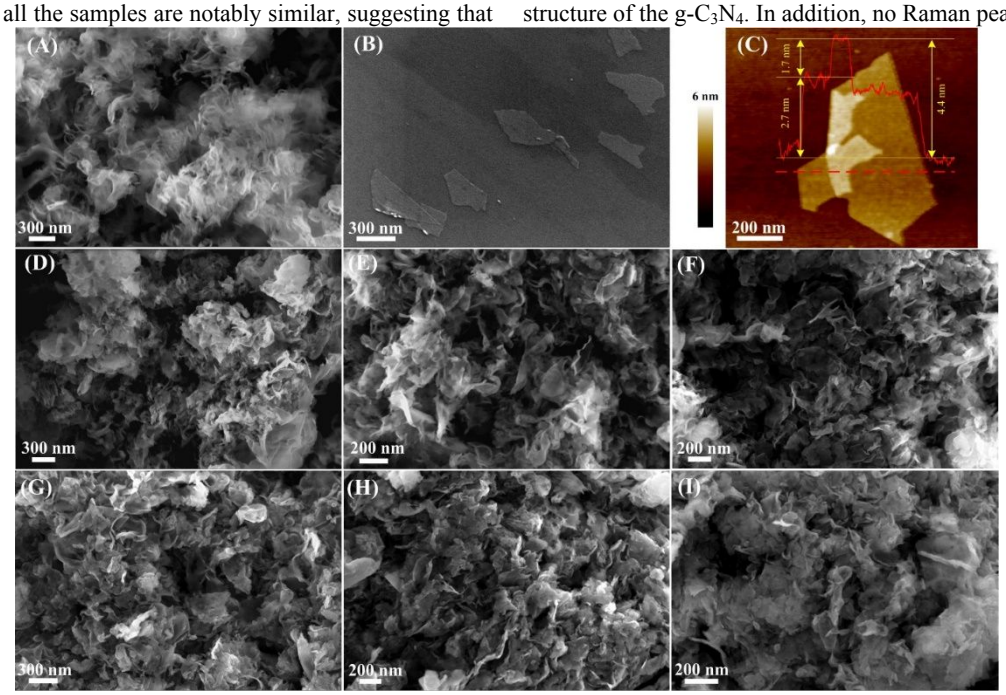

Figure 1. SEM images of g-C_3N_4 nanosheets (A), monolayer Ti_3C_2 (B), P-g-C_3N_4 (D), 1-TC/CN (E), 2-TC/CN (F), 3-TC/CN (G), 4-TC/CN (H), and 5-TC/CN (I); AFM image (C) of a representative monolayer Ti_3C_2 deposited on Si wafe.

detected in the Ti_3C_2/g-C_3N_4 composites due to its low concentration, which is consistent with the XRD results.

g-C_3N_4 nanosheets and monolayer Ti_3C_2 were successfully prepared from bulk g-C_3N_4 and Ti_3AlC_2, respectively. The SEM images of the bulk g-C_3N_4 and Ti_3AlC_2 are shown in Figure S4C and Figure S6A, and the SEM images of g-C_3N_4 nanosheets and monolayer Ti_3C_2 are shown in Figure 1A and B, respectively. Figure 1A shows the sheet structure of g-C_3N_4, which indicates that the bulk g-C_3N_4 was split into small nanosheets during thermal exfoliation at 550 °C. After the thermal exfoliation, the g-C_3N_4 nanosheets display a lighter yellow color if compared to that of bulk g-C_3N_4 (Figure S4A and B, Supporting Information). The flake-shaped morphology of Ti_3C_2 is displayed in Figure 1B; these Ti_3C_2 flakes show clean surfaces and sizes ranging from dozens of nanometers to hundreds of nanometers. The thickness of the Ti_3C_2 flakes was investigated by AFM (Figure 1C). From the AFM height profile (Figure S5, Supporting Information) measured along the red dashed line in Figure 1C, the height of the folded region relative to the layer underneath was measured as 1.7 nm, which corresponds to a monolayer Ti_3C_2.[38] The thickness of the Ti_3C_2 flakes relative to the Si substrate is 2.7 nm, which is possibly due to the surface adsorbates (such as water molecules) present between the Ti_3C_2 flakes and the Si substrate.[38] The typical Tyndall effect was clearly observed in an aqueous suspension of Ti_3C_2 flakes (Figure S6B, Supporting Information), demonstrating their excellent hydrophilicity and dispersity.[45] In addition, the thickness of Ti_3C_2 flakes obtained from AFM range from 1.7 nm to 2.6 nm (Figure S6C and D, Supporting Information), indicating that all the flakes are monolayer Ti_3C_2.

The morphology of the protonated g-C_3N_4 and the 2D/2D Ti_3C_2/g-C_3N_4 composites was investigated by SEM (Figure 1). After the ultrasonic treatment in an aqueous HCl solution, the sheet-like structure of g-C_3N_4 remains unchanged (Figure 1D). However, these g-C_3N_4 nanosheets stacked together after drying at 80 °C, and the BET specific surface area of the g-C_3N_4 nanosheet decreased from 153.6 $m^2\ g^{-1}$ to 79.0 $m^2\ g^{-1}$ according to N_2 adsorption-desorption analysis (Figure S7 and Table S1, Supporting Information). In addition, the Ti_3C_2/g-C_3N_4 composites with different content of Ti_3C_2 are composed of thin nanosheets (Figure 1E, F, G, H, and I). The BET specific surface area of the 1-TC/CN, 2-TC/CN, 3-TC/CN, 4-TC/CN, and 5-TC/CN samples are 73.8, 76.6, 82.2, 83.1, and 84.3 $m^2\ g^{-1}$, respectively (Figure S7 and Table S1, Supporting Information). Because Ti_3C_2 and g-C_3N_4 are both thin flakes, it is hard to distinguish the Ti_3C_2 and g-C_3N_4 from the SEM images of the Ti_3C_2/g-C_3N_4 composites. The EDS elemental mapping verifies the presence of C, N, and Ti element in the Ti_3C_2/g-C_3N_4 composites, which demonstrates that the composites are composed of Ti_3C_2 and g-C_3N_4 (Figure S8, Supporting Information).

Nanoscale

ARTICLE

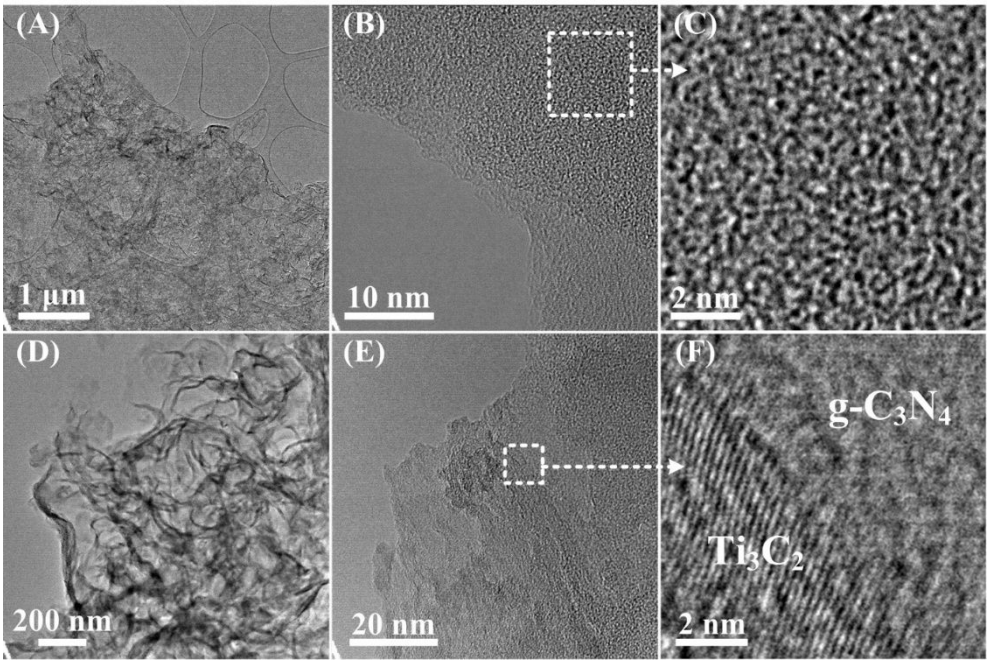

Figure 2. TEM and HRTEM images of g-C_3N_4 (A, B, C) and 3-TC/CN (D, E, F).

To better understand the morphology and microstructure of the as-synthesized photocatalysts, the g-C_3N_4 and 3-TC/CN samples were further investigated by TEM and HRTEM (Figure 2). The TEM images of the g-C_3N_4 exhibit a 2D morphology (Figure 2A), implying the ultrathin structures of g-C_3N_4 nanosheets. As shown in Figure 2B and C, the g-C_3N_4 had low crystallinity and was mostly amorphous, which is consistent with previous reports.[46, 47] After the g-C_3N_4 nanosheets were combined with monolayer Ti_3C_2, the Ti_3C_2/g-C_3N_4 composites still displayed the sheet-shape morphology (Figure 2D). The HRTEM images of the Ti_3C_2/g-C_3N_4 composites display large two-dimensional structures consisting of flat irregularly shaped nanosheets of 2D/2D structures. Additionally, an obvious composite structure can be seen in the HRTEM image of 3-TC/CN, as shown in Figure 2E and F. The clear lattice fringes were assigned to Ti_3C_2 flakes, whereas the disordered areas were ascribed to the g-C_3N_4 nanosheets. Notably, an obvious intimate interface was observed between Ti_3C_2 and g-C_3N_4 suggesting the formation of 2D/2D Ti_3C_2/g-C_3N_4 heterojunctions, which is in accordance with the EDS analysis. This 2D/2D Ti_3C_2/g-C_3N_4 interface is beneficial to the transfer of photoinduced electrons from g-C_3N_4 to Ti_3C_2 due to the excellent electronic conductivity of the Ti_3C_2.

The chemical composition and oxidation state of the g-C_3N_4 and 3-TC/CN samples were characterized by XPS, as shown in Figure 3. C and N elements were detected in the XPS survey spectrum of the g-C_3N_4 sample (Figure S9A, Supporting Information), and the C and N elements were further investigated by the high resolution XPS (Figure 3A and B). There are three carbon species in the C 1s spectra of the g-C_3N_4 sample. The 284.8 eV peak was assigned to the adsorbed carbon species (C-C) on the g-C_3N_4 surface, and the 286.8 eV and 288.0 eV peaks can be ascribed to the sp^2-hybridized carbon in triazine rings (C-N=C) and N-contained aromatic ring (N-C=N), respectively. The carbon in N-C=N is considered as the major carbon species in g-C_3N_4 nanosheets.[48] Three peaks were observed in the N 1s spectrum (Figure 3B), and the peaks located at binding energies of 398.9, 400.6, and 401.5 eV can be attributed to the sp2-hybridized nitrogen involved in the triazine rings (C-N=C), the tertiary nitrogen N-$(C)_3$ groups, and the free amino groups (C-N-H), respectively.[48, 49] Ti, N, and C elements can be observed in the XPS survey spectrum of 3-TC/CN (Figure S9B, Supporting Information), indicating that Ti_3C_2 and g-C_3N_4 are present in the composite. The high resolution spectra of Ti 2p, N 1s, and C 1s are shown in Figure 3C, D and E, and the XPS peak fitting results are displayed in Table S2. As shown in Figure 3C, the peaks located at 454.9 (461.2), 455.9 (462.0), and 457.2 eV (463.4 eV) belong to the Ti (I,II, or IV), Ti^{2+}(I,II, or IV), and Ti^{3+}(I,II, or IV) species in the Ti_3C_2, respectively, indicating the existence of Ti_3C_2 in the 3-TC/CN sample. Furthermore, the peaks located at 459.4 eV (465.6 eV) correspond to the Ti in the $TiO_{2-x}F_x$ species, which are likely originated from the slight oxidation of the Ti_3C_2.[50] The C 1s spectrum exhibits four peaks at 281.4, 284.7, 286.8, and 288.0 eV. The peaks at 281.4 eV correspond to C-Ti-T_x(I, II, III or IV) species of Ti_3C_2, which further confirms the presence of the Ti_3C_2.[50] In addition, the peaks at 284.8, 286.8, and 288.0 eV can be assigned to

Nanoscale

ARTICLE

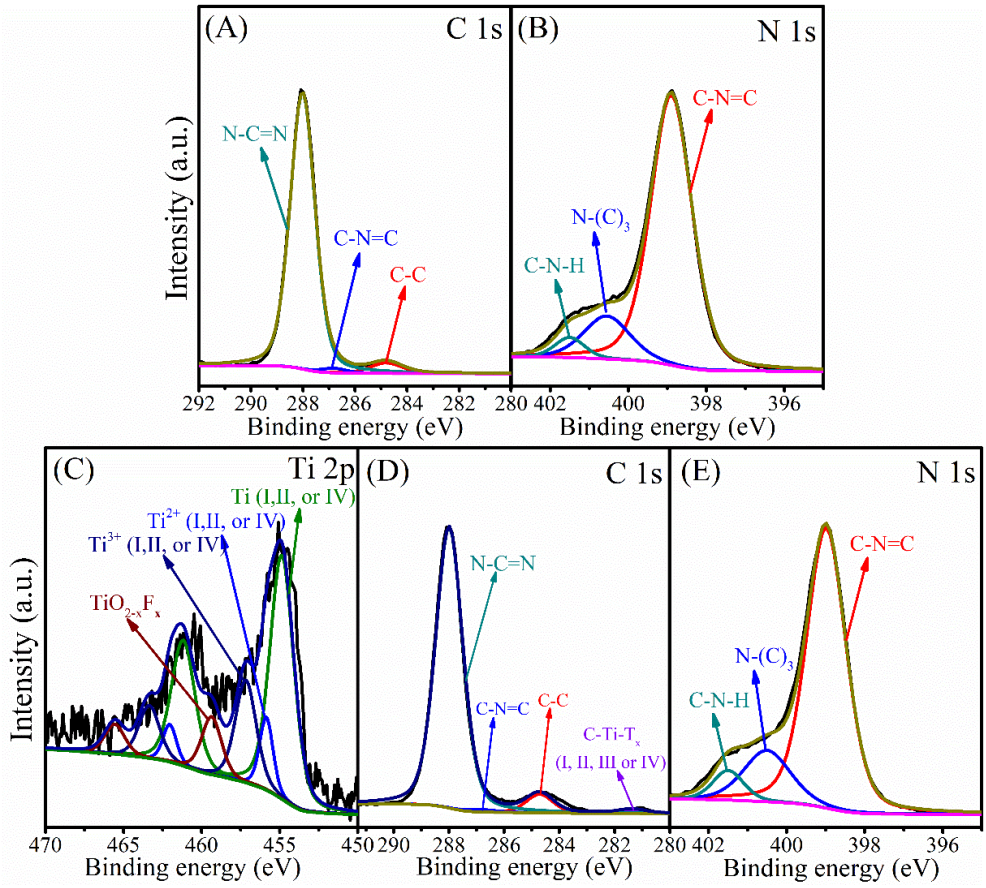

Figure 3. XPS spectra of C 1s (A) and N 1s (B) in g-C_3N_4, and Ti 2p (C), C 1s (D) and N 1s (E) in 3-TC/CN.

the carbon in C-C, C-N=C, and N-C=N, which is similar to the peaks in the XPS spectra of g-C_3N_4 sample. Moreover, the high resolution spectra of N 1s in the 3-TC/CN sample are in accordance with that of g-C_3N_4. The above analysis demonstrates that the loading of Ti_3C_2 did not change the structure and chemical composition of the g-C_3N_4, and the 3-TC/CN composite is consist of both Ti_3C_2 and g-C_3N_4. The XPS and TEM analyses indicate that the 2D/2D heterojunction of Ti_3C_2/g-C_3N_4 was successfully formed by the electrostatic self-assembly method.

The optical absorption properties of the photocatalyst play an important role in their activity. The UV-vis absorption spectra of as-synthesized photocatalysts are shown in Figure 4A and Figure S10. The g-C_3N_4 nanosheets show a clear blue shift of the intrinsic absorption edge compared with that of bulk g-C_3N_4. Moreover, the band gap of bulk g-C_3N_4 (B-g-C_3N_4) and the g-C_3N_4 nanosheets is 2.57 and 2.77 eV, respectively, as determined from the $(ahv)^{1/2}$ versus photon-energy plots (Figure S10, Supporting Information). When B-g-C_3N_4 is exfoliated to ultrathin g-C_3N_4 nanosheets, the band gap increases due to the quantum confinement effect by shifting the conduction and valence band edges in opposite directions, which is identical with the previous reports.[51, 52] It can be seen from Figure 4A that all the Ti_3C_2/g-C_3N_4 composites exhibit enhanced light absorption compared to the pure g-C_3N_4 nanosheets. With the increase of Ti_3C_2 content, the absorption intensity of Ti_3C_2/g-C_3N_4 composites gradually increased within the range of 250~800 nm. Such increased light absorption is attributed to the full-spectrum absorption of dark Ti_3C_2. Although the enhanced light absorption might not be able to excite the photoelectrons and holes in Ti_3C_2/g-C_3N_4 composites, it is likely to facilitate the surface catalytic reactions by converting light energy to heat to activate the catalyst,[53] due to the efficient photothermal conversion characteristics of Ti_3C_2.[45, 54]

Photoluminescence (PL) spectroscopy represents a useful tool to understand the destiny of electron-hole pairs in photocatalysts, as PL emission is caused by the recombination of electrons and holes. Therefore, a low PL intensity generally indicates a high separation efficiency of electron-hole pairs.[55, 56] As shown in Figure 4B, the PL intensity of the 3-TC/CN decreased significantly compared with that of pure g-C_3N_4 nanosheets, indicating that radiative recombination of

Nanoscale

ARTICLE

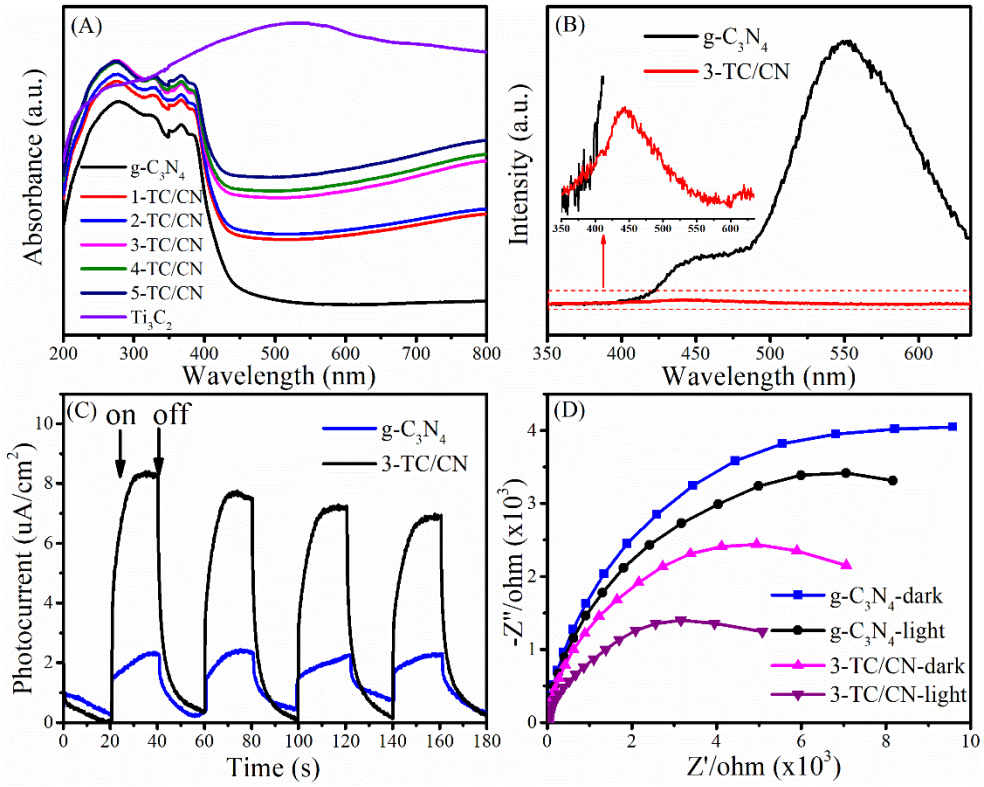

Figure 4. UV-vis absorption spectra of different photocatalysts (A), PL spectra of g-C_3N_4 and 3-TC/CN (B), transient photocurrent (C) and Nyquist plots (D) of g-C_3N_4 and 3-TC/CN in the darkness or under visible light irradiation.

charge carriers was suppressed. Notably, there are two obvious peaks located at around 445 and 550 nm in the PL spectrum of g-C_3N_4. The peak centred at 445 nm can be attributed to the band-band transition, which matches well with the absorption edge of the g-C_3N_4 from UV-Vis absorption measurements. While the peak at 550 nm may be due to the radiative recombination from the shallow trapped electrons, indicating the presence of sub-gap defects in the g-C_3N_4 nanosheets. Similar phenomenon was found in the previous reports.[57-59] When the g-C_3N_4 nanosheets were combined with the Ti_3C_2 flakes, a 2D/2D intimate interface was formed, such a 2D/2D interface provides maximum contact surface between the g-C_3N_4 nanosheets and the Ti_3C_2 flakes. Furthermore, due to the high electrical conductivity of the metallic Ti_3C_2, the photogenerated electrons can easily transfer from the g-C_3N_4 nanosheets to the Ti_3C_2 flakes instead of to the defect states, resulted in the elimination of the main peak at 550 nm and the significantly lowered PL intensity. Such an electron transfer path is beneficial to the separation of photoelectrons and holes.

In order to shed more light on the charge transfer in the photocatalysts, transient photocurrent response and electrochemical impedance spectra (EIS) were collected for typical samples. As shown in Figure 4C, the photocurrent intensity for 3-TC/CN is about four times stronger than that of pristine g-C_3N_4 when the light is on, indicating the better charge transfer efficiency within the ultrathin 2D/2D Ti_3C_2/g-C_3N_4 nanosheets. Figure 4D shows the Nyquist plots of g-C_3N_4 and 3-TC/CN in the darkness or under visible light irradiation. It is well known that smaller arc radius of the Nyquist plot indicates lower electric charge transfer resistance in the samples.[60] The arc radius of g-C_3N_4 and 3-TC/CN under visible light irradiation was obviously smaller than those in the darkness, which suggests the generation of photogenerated carriers in the samples. Moreover, the arc radius of 3-TC/CN sample was distinctly smaller than that of g-C_3N_4, further confirming the better charge transfer ability within the 3-TC/CN. Such enhanced charge transfer efficiency is likely due to the efficient interfacial charge transfer upon the 2D/2D heterojunction of ultrathin Ti_3C_2/g-C_3N_4 nanosheets. In the 2D/2D Ti_3C_2/g-C_3N_4 system, the metallic Ti_3C_2 is not able to generate the photoelectrons and holes under visible light irradiation. However, the Ti_3C_2 can be used as the electron acceptor to capture the photoelectrons generated by the g-C_3N_4 due to its excellent electrical conductivity, which can effectively suppress the recombination of photoinduced charge carriers.

The activity of all as-prepared samples was evaluated by photocatalytic hydrogen evolution from water under visible light irradiation (＞400 nm), with triethanolamine (TEOA) as the hole scavenger. Control experiments indicate that no hydrogen was produced in the absence of photocatalyst or light irradiation. As displayed in Figure 5A and B, the coupling of Ti_3C_2 flakes with g-C_3N_4 nanosheets leads to a remarkable enhancement in the photocatalytic hydrogen evolution rate. Pristine g-C_3N_4 nanosheets showed a very low hydrogen evolution rate of 7.1 μmol h^{-1} g_{cat}^{-1}, which is comparatively in consistent with the literature values.[61, 62] In

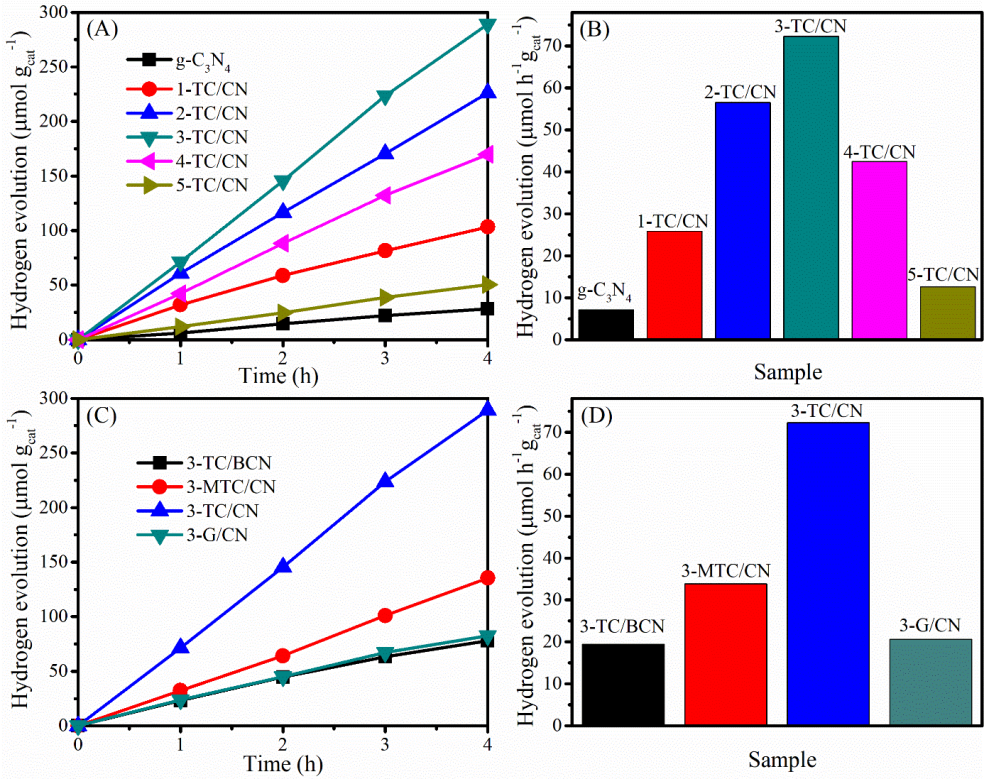

Figure 5. Photocatalytic hydrogen evolution over g-C_3N_4, 1-TC/CN, 2-TC/CN, 3-TC/CN, 4-TC/CN, 5-TC/CN, 3-TC/BCN, 3-MTC/CN, and 3-G/CN.

contrast, when the g-C_3N_4 nanosheets combined with small content of Ti_3C_2 flakes (1.0 wt%), the photocatalytic activity of 1-TC/CN was obviously increased to 25.8 μmol h^{-1} g_{cat}^{-1}. With the increase of the content of Ti_3C_2 flakes, the photocatalytic hydrogen evolution rate of the Ti_3C_2/g-C_3N_4 composites is gradually improved.

The optimized sample 3-TC/CN shows the highest hydrogen production rate of 72.3 μmol h^{-1} g_{cat}^{-1}, which is more than 10 times higher than that of pristine g-C_3N_4. Moreover, the hydrogen production rate of 3-TC/CN is higher than that of the 3.0 wt% MWNTs/g-C_3N_4 (64.1 μmol h^{-1} g_{cat}^{-1}) and 1.0 wt% Pt/g-C_3N_4 (20.3 μmol h^{-1} g_{cat}^{-1}) under visible light (＞400 nm).[63] Such enhanced activity can be ascribed to the formation of 2D/2D compact interfaces in the ultrathin Ti_3C_2/g-C_3N_4 nanosheets. Under visible light irradiation, the photogenerated electrons produced on the conduction band of the g-C_3N_4 can effectively transfer via the 2D/2D interfaces and accumulate on the metallic Ti_3C_2, due to the short charge transfer distance and the large and compact contact surface. As a consequence, the recombination of the photogenerated electrons and holes was impeded and the photocatalytic activity of g-C_3N_4 was enhanced. However, the hydrogen production rate of the 3-TC/CN is still lower than that of the 3.0 wt% Pt/g-C_3N_4 (175.6 μmol h^{-1} g_{cat}^{-1}) under the same experimental conditions (Figure S11, Supporting Information), which might be due to the less active sites on 3-TC/CN than the 3.0 wt% Pt/g-C_3N_4. Notably, increasing the content of Ti_3C_2 flakes past 3.0 wt% decreases the photocatalytic activity of g-C_3N_4. Such reduced activity is due to the excessive amount of Ti_3C_2 flakes hindering the light absorption of g-C_3N_4. Nevertheless, the 5-TC/CN sample still shows higher photocatalytic activity (12.6 μmol h^{-1} g_{cat}^{-1}) than that of the pristine g-C_3N_4. Moreover, no hydrogen can be detected when the Ti_3C_2 was used as the photocatalyst under visible light irradiation, indicating the photocatalytic reaction cannot be evoked by the Ti_3C_2 alone due to its metallic character. This result further confirms that the role of Ti_3C_2 is an electron acceptor and co-catalyst rather than a photocatalyst.

In comparison, under the same experimental conditions and with the same loading (3.0 wt.%), 3-TC/BCN, 3-MTC/CN, and 3-G/CN were prepared and used in the photocatalytic hydrogen evolution reaction (Figure 5C and D). The SEM images of the multilayer Ti_3C_2 (M-Ti_3C_2) and monolayer graphene can be found in Figure S12. In addition, the XRD patterns and the UV-vis absorption spectra of the 3-TC/BCN, 3-MTC/CN, and 3-G/CN samples can be seen in Figure S13. As shown in Figure 5C and D, 3-G/CN shows higher photocatalytic activity (20.7 μmol h^{-1} g_{cat}^{-1}) than that of pristine g-C_3N_4 (7.1 μmol h^{-1} g_{cat}^{-1}) and shows much lower activity than that of 3-TC/CN (72.3 μmol h^{-1} g_{cat}^{-1}). Graphene has been widely used as an electron acceptor for photocatalysts to enhance their photocatalytic

Nanoscale

ARTICLE

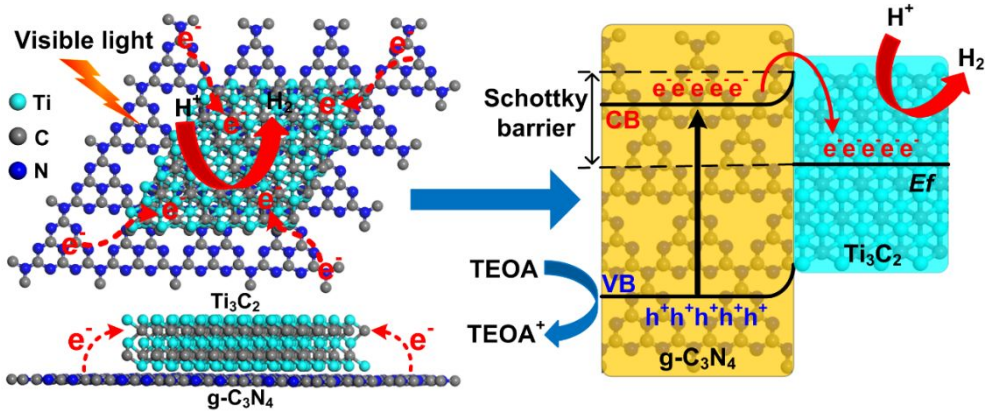

Figure 6. Proposed mechanism of photocatalytic hydrogen evolution over the Ti_3C_2/g-C_3N_4 system.

activity due to its good electrical conductivity. Herein, the lower activity of 3-G/CN than 3-TC/CN may be attributed to the following reasons: (1) O-terminated Ti_3C_2 with a low content of –OH and –F terminal groups was obtained by the LiF/HCl etching method,[64] and the O-terminated MXenes have high work functions between 5.75 and 6.25 eV,[65] which is much higher than that of graphene (4.5 eV).[66, 67] (2) The Gibbs free energy for hydrogen adsorption (ΔG_H) on graphene is 0.79 eV,[68] while the O-terminated Ti_3C_2 shows a near-zero value of $\Delta G_H = 0.00283$ eV at the same H* coverage ($\theta = 1/2$), indicating that the O-terminated Ti_3C_2 is superior for H_2 evolution reaction.[33] (3) The hydrophobic nature of pure graphene is adverse to the adsorption of water molecules and is unfavorable for the hydrogen evolution from water.[69, 70] On the contrary, Ti_3C_2 possesses numerous hydrophilic functionalities (–OH and –O) on its surface, which can promote its strong interaction with water molecules.[71] (4) Graphene is made of nothing but carbon. However, the Ti_3C_2 is consist of carbon and titanium, and the exposed terminal metal sites on the Ti_3C_2 might lead to stronger redox reactivity than that of the carbon materials.[33] (5) The higher work functions of O-terminated Ti_3C_2 than that of graphene resulted in a higher Schottky barrier in 3-TC/CN than that in 3-G/CN.[32] Thus the separation efficiency of the photogenerated electrons and holes in 3-TC/CN is higher than that of 3-G/CN, and this is confirmed by PL analysis (Figure S14, Supporting Information).

In order to reveal whether the formation of 2D/2D heterojunction is the key factor for the enhanced photocatalytic activity or not, the photocatalytic activities of the 3-TC/BCN (2D/0D) and 3-MTC/CN (0D/2D) samples were investigated and compared with that of 3-TC/CN (2D/2D). Figure 5C and D shows that the 3-TC/BCN and 3-MTC/CN samples exhibit much lower photocatalytic hydrogen production rate than that of 3-TC/CN sample, which suggests that the 2D/2D heterojunction of photocatalysts is more beneficial to suppress the recombination of photoinduced electrons and holes, thus enhancing the performance of photocatalysts. The advantage of the 2D/2D heterojunction has also been reported on the other 2D photocatalysts.[1, 46] In addition, the apparent quantum yield (400 nm) of the g-C_3N_4, 1-TC/CN, 2-TC/CN, 3-TC/CN, 4-TC/CN, 5-TC/CN, 3-TC/BCN, 3-MTC/CN and 3-G/CN was 0.08%, 0.29%, 0.63%, 0.81%, 0.47%, 0.14%, 0.22%, 0.38% and 0.23%, respectively.

The photochemical stability of a photocatalyst is very important for photocatalytic hydrogen evolution. Therefore, the photocatalytic stability of the optimal sample (3-TC/CN) was investigated (Figure S15A, Supporting Information). After 3 cycles (reaction for 28 h), the photocatalytic hydrogen evolution rate of the 3-TC/CN did not show a remarkable decrease in activity, indicating its photochemical stability. To further study the stability of 3-TC/CN, XRD, SEM, UV-vis absorption and N_2 adsorption-desorption was used to characterize the 3-TC/CN sample after photocatalysis. From the XRD pattern of the 3-TC/CN (Figure S15B, Supporting Information), no obvious change can be observed, suggesting the composition and structure of the 3-TC/CN was maintained after reaction. Figure S15C shows that the light absorption of the 3-TC/CN decreased slightly after reaction, which is probably due to the separation of Ti_3C_2 flakes from the g-C_3N_4 nanosheets. Since the 2D/2D Ti_3C_2/g-C_3N_4 composites are prepared by the electrostatic self-assembly method, some Ti_3C_2 might not be able to bind with g-C_3N_4 tightly. Therefore, a long reaction with agitation might cause some Ti_3C_2 to separate from the Ti_3C_2/g-C_3N_4 composites, which leads to the deactivation of the photocatalysts. The BET specific surface area of the 3-TC/CN before and after reaction is 82.0 and 83.1 $m^2\ g^{-1}$, respectively, which further confirms the stable nanosheet structure of the 3-TC/CN (Figure S15D, Supporting Information). Moreover, the nanosheet morphology of the 3-TC/CN samples did not change according to the SEM images of 3-TC/CN (Figure S16, Supporting Information). Besides, X-ray photoelectron spectra of the used 3-TC/CN indicate that no remarkable changes can be observed on the binding energies of Ti, C, and N, indicating the

excellent chemical stability of the Ti_3C_2/g-C_3N_4 composites (Figure S17 and Table S3, Supporting Information).

According to the above results and discussion, a mechanism of 2D/2D Ti_3C_2/g-C_3N_4 for photocatalytic hydrogen evolution under visible light irradiation is proposed and illustrated in Figure 6. Under light irradiation, the electrons in the valence band (VB) of g-C_3N_4 can be excited to the conduction band (CB), generating photoinduced electrons and holes. Due to the excellent electronic conductivity of Ti_3C_2, the large intimate 2D/2D interface between the Ti_3C_2 and g-C_3N_4 and the short charge transfer distance, the migration rate of the photoinduced electrons can be greatly improved. In addition, the conduction band potential of the g-C_3N_4 was determined to be around -1.02 V vs NHE using the Mott-Schottky plots.[10, 72-74] Besides, the Ti_3C_2 obtained from the LiF/HCl etching method should be O-terminated,[65] and the Fermi level of the O-terminated Ti_3C_2 was theoretically determined to be 0.71 eV vs NHE.[53] Therefore, the most positive Fermi level of O-terminated Ti_3C_2 exhibits great ability to capture photoinduced electrons from the CB of the g-C_3N_4 and the holes was left on the VB of g-C_3N_4, which will significantly enhance the separation of electrons and holes.[35] Moreover, a Schottky junction can be formed due to the close contact in 2D/2D Ti_3C_2/g-C_3N_4.[35] In this case, the role of Ti_3C_2 as an electron receiver promotes the electrons transfer from g-C_3N_4 to Ti_3C_2. Therefore, the photogenerated electrons were accumulated on the Ti_3C_2 and the H^+ is reduced to H_2 on the surface of the Ti_3C_2. At the same time, the holes in the VB of g-C_3N_4 are used to oxidize TEOA into $TEOA^+$. Thus, the photoinduced electrons and holes can be effectively separated and transferred in the 2D/2D Ti_3C_2/g-C_3N_4, which leads to remarkable enhancement of photocatalytic performance.

Furthermore, the O-terminated Ti_3C_2 shows a near-zero value of Gibbs free energy for hydrogen adsorption ($\triangle G_H$=0.00283 eV) at the H* coverage of 1/2 according to theoretical calculations,[33] thus the H^+ can be facilely reduced to H_2 on the Ti_3C_2 surface. The hydrophilic functionalities and the exposed terminal metal sites on the Ti_3C_2 might also be beneficial to enhance the photocatalytic performance of the Ti_3C_2/g-C_3N_4. It is noted that the light adsorption of the Ti_3C_2/g-C_3N_4 composites is enhanced due to the dark color nature of Ti_3C_2. Although the enhanced light adsorption is unlikely to excite more photoinduced electrons and holes, the photothermal effect of Ti_3C_2 can convert light to heat.[45, 54] According to previous reports, the photocatalytic hydrogen production rate can be enhanced by heating of the reaction system, indicating the photothermal effect is related to the energy required for photocatalytic reaction.[75] Moreover, the temperature of the photocatalyst can be increased and provide energy to activate reactant and boost the local photocatalytic reaction.[53, 76] In our current study, the reactor is kept at a constant temperature of 25 °C with a cooling recirculator. Yet the photothermal effect of Ti_3C_2 at local scale can still be potentially present and favorable for activating the photocatalysts and improving the photocatalytic hydrogen evolution efficiency.[35]

Conclusions

In summary, the 2D/2D Ti_3C_2/g-C_3N_4 nanosheets were successfully prepared by the electrostatic self-assembly approach. The formation of the 2D/2D heterojunctions in the Ti_3C_2/g-C_3N_4 composites was demonstrated. The photocatalytic hydrogen evolution rate of the optimized 2D/2D Ti_3C_2/g-C_3N_4 (3-TC/CN) was over 10 times higher than that of the pure g-C_3N_4. The superior activity of the 3-TC/CN was attributed to the 2D/2D intimate contact between the monolayer Ti_3C_2 and the g-C_3N_4 nanosheets. The 2D/2D interfaces provided a large charge transfer channel for accelerating the photoinduced electrons transfer from the conduction band of g-C_3N_4 to the metallic Ti_3C_2. Moreover, the construction of the Schottky junction further promoted the separation of the photogenerated electrons and holes, which will greatly enhance the photocatalytic activity of the g-C_3N_4. We believe that this work will stimulate ongoing interest in utilizing 2D MXene as co-catalysts to improve the performance of photocatalysts for hydrogen evolution as well as other reactions.

Conflicts of interest

There are no conflicts to declare.

Acknowledgements

This research was supported and conducted at the Center for Nanophase Materials Sciences, which is a DOE Office of Science User Facility. TMS acknowledges the support from China Scholarship Council. ZDH gratefully acknowledges a Graduate Research Fellowship award from the National Science Foundation (DGE-1650044). LB acknowledges financial support from National Science Foundation supplemental intern funding 1511818.

References

1. S. Liu, F. Chen, S. Li, X. Peng and Y. Xiong, *Appl. Catal. B: Environ.*, 2017, **211**, 1-10.
2. T. Su, Q. Shao, Z. Qin, Z. Guo and Z. Wu, *ACS Catal.*, 2018, **8**, 2253-2276.
3. X. Li, S. Liu, K. Fan, Z. Liu, B. Song and J. Yu, *Adv. Energy Mater.*, 2018, **8**, 1800101.
4. Y. Jia, D. Zhao, M. Li, H. Han and C. Li, *Chin. J. Catal.*, 2018, **39**, 421-430.
5. R. Shi, H.-F. Ye, F. Liang, Z. Wang, K. Li, Y. Weng, Z. Lin, W.-F. Fu, C.-M. Che and Y. Chen, *Adv. Mater.*, 2018, **30**, 1705941.
6. P.-Y. Kuang, P.-X. Zheng, Z.-Q. Liu, J.-L. Lei, H. Wu, N. Li and T.-Y. Ma, *Small*, 2016, **12**, 6735-6744.
7. M. Ahmed and G. Xinxin, *Inorg. Chem. Front.*, 2016, **3**, 578-590.
8. S. Zhao, Y. Zhang, Y. Zhou, Y. Wang, K. Qiu, C. Zhang, J. Fang and X. Sheng, *Carbon*, 2018, **126**, 247-256.
9. J. Fu, J. Yu, C. Jiang and B. Cheng, *Adv. Energy Mater.*, 2018, **8**, 1701503.
10. M. Zhu, S. Kim, L. Mao, M. Fujitsuka, J. Zhang, X. Wang and T. Majima, *J. Am. Chem. Soc.*, 2017, **139**, 13234-13242.
11. Y. Yu, Y. Wei, W. Xiaofang, L. Pei, G. Wenyu, Z. Haihan, W. Songmei and D. Kejian, *Adv. Mater.*, 2018, **30**, 1705060.
12. L. Lin, W. Ren, C. Wang, A. M. Asiri, J. Zhang and X. Wang, *Appl. Catal. B: Environ.*, 2018, **231**, 234-241.
13. L. Lin, Z. Yu and X. Wang, *Angew. Chem. Int. Ed.*, 2018, DOI: 10.1002/anie.201809897.

14. Y. Wang, S. Zhao, Y. Zhang, J. Fang, Y. Zhou, S. Yuan, C. Zhang and W. Chen, *Appl. Surf. Sci.*, 2018, **440**, 258-265.
15. R. Ma, L. Dong, B. Li, T. Su, X. Luo, Z. Qin and H. Ji, *ChemistrySelect*, 2018, **3**, 5891-5899.
16. S. P. Adhikari, Z. D. Hood, Vincent W. Chen, K. L. More, K. Senevirathne and A. Lachgar, *Sustain. Energ. Fuel*, 2018, **2**, 2507-2515.
17. S. P. Adhikari, Z. D. Hood, K. L. More, V. W. Chen and A. Lachgar, *ChemSusChem*, 2016, **9**, 1869-1879.
18. Y. Zheng, Z. Yu, H. Ou, A. M. Asiri, Y. Chen and X. Wang, *Adv. Funct. Mater.*, 2018, **28**, 1705407.
19. L. Kong, Y. Ji, Z. Dang, J. Yan, P. Li, Y. Li and S. Liu, *Adv. Funct. Mater.*, 2018, **28**, 1800668.
20. R.-B. Wei, Z.-L. Huang, G.-H. Gu, Z. Wang, L. Zeng, Y. Chen and Z.-Q. Liu, *Appl. Catal. B: Environ.*, 2018, **231**, 101-107.
21. Y.-J. Yuan, Y. Yang, Z. Li, D. Chen, S. Wu, G. Fang, W. Bai, M. Ding, L.-X. Yang, D.-P. Cao, Z.-T. Yu and Z.-G. Zou, *ACS Appl. Energy Mater.*, 2018, **1**, 1400-1407.
22. G. Zhang, Z.-A. Lan, L. Lin, S. Lin and X. Wang, *Chem. Sci.*, 2016, **7**, 3062-3066.
23. M. Naguib, M. Kurtoglu, V. Presser, J. Lu, J. Niu, M. Heon, L. Hultman, Y. Gogotsi and M. W. Barsoum, *Adv. Mater.*, 2011, **23**, 4248-4253.
24. Y. Xia, T. S. Mathis, M.-Q. Zhao, B. Anasori, A. Dang, Z. Zhou, H. Cho, Y. Gogotsi and S. Yang, *Nature*, 2018, **557**, 409-412.
25. C. Chen, X. Xie, B. Anasori, A. Sarycheva, T. Makaryan, M. Zhao, P. Urbankowski, L. Miao, J. Jiang and Y. Gogotsi, *Angew. Chem. Int. Ed.*, 2018, **57**, 1846-1850.
26. K. Huang, Z. Li, J. Lin, G. Han and P. Huang, *Chem. Soc. Rev.*, 2018, **47**, 5109-5124.
27. W. Yuan, L. Cheng, Y. An, H. Wu, N. Yao, X. Fan and X. Guo, *ACS Sustain. Chem. Eng.*, 2018, **6**, 8976-8982.
28. G. Gao, A. P. O'Mullane and A. Du, *ACS Catal.*, 2017, **7**, 494-500.
29. X. Yang, N. Gao, S. Zhou and J. Zhao, *Phys. Chem. Chem. Phys.*, 2018, **20**, 19390-19397.
30. S. Li, P. Tuo, J. Xie, X. Zhang, J. Xu, J. Bao, B. Pan and Y. Xie, *Nano Energy*, 2018, **47**, 512-518.
31. T. Su, R. Peng, Z. D. Hood, M. Naguib, I. N. Ivanov, J. K. Keum, Z. Qin, Z. Guo and Z. Wu, *ChemSusChem*, 2018, **11**, 688-699.
32. H. Wang, R. Peng, Z. D. Hood, M. Naguib, S. P. Adhikari and Z. Wu, *ChemSusChem*, 2016, **9**, 1490-1497.
33. J. Ran, G. Gao, F.-T. Li, T.-Y. Ma, A. Du and S.-Z. Qiao, *Nat. Commun.*, 2017, **8**, 13907.
34. Y. Sun, D. Jin, Y. Sun, X. Meng, Y. Gao, Y. Dall'Agnese, G. Chen and X.-F. Wang, *J. Mater. Chem. A*, 2018, **6**, 9124-9131.
35. X. An, W. Wang, J. Wang, H. Duan, J. Shi and X. Yu, *Phys. Chem. Chem. Phys.*, 2018, **20**, 11405-11411.
36. B. Lin, H. Li, H. An, W. Hao, J. Wei, Y. Dai, C. Ma and G. Yang, *Appl. Catal. B: Environ.*, 2018, **220**, 542-552.
37. M. Zhang, J. Qin, S. Rajendran, X. Zhang and R. Liu, *ChemSusChem*, 2018, **11**, 4226-4236.
38. A. Lipatov, M. Alhabeb, M. R. Lukatskaya, A. Boson, Y. Gogotsi and A. Sinitskii, *Adv. Electron. Mater.*, 2016, **2**, 1600255.
39. Y. Kang, Y. Yang, L.-C. Yin, X. Kang, G. Liu and H.-M. Cheng, *Adv. Mater.*, 2015, **27**, 4572-4577.
40. W.-J. Ong, L.-L. Tan, S.-P. Chai, S.-T. Yong and A. R. Mohamed, *Nano Energy*, 2015, **13**, 757-770.
41. C. E. Ren, K. B. Hatzell, M. Alhabeb, Z. Ling, K. A. Mahmoud and Y. Gogotsi, *J. Phys. Chem. Lett.*, 2015, **6**, 4026-4031.
42. B. Tahir, M. Tahir and N. A. S. Amin, *Appl. Surf. Sci.*, 2017, **419**, 875-885.
43. Z. A. Lan, G. G. Zhang and X. C. Wang, *Appl. Catal. B: Environ.*, 2016, **192**, 116-125.
44. H. Yu, L. Shang, T. Bian, R. Shi, G. I. N. Waterhouse, Y. Zhao, C. Zhou, L.-Z. Wu, C.-H. Tung and T. Zhang, *Adv. Mater.*, 2016, **28**, 5080-5086.
45. H. Lin, X. Wang, L. Yu, Y. Chen and J. Shi, *Nano Lett.*, 2017, **17**, 384-391.
46. Q. Wang, W. Wang, L. Zhong, D. Liu, X. Cao and F. Cui, *Appl. Catal. B: Environ.*, 2018, **220**, 290-302.
47. F. Cheng, H. Wang and X. Dong, *Chem. Commun.*, 2015, **51**, 7176-7179.
48. Q. Y. Lin, L. Li, S. J. Liang, M. H. Liu, J. H. Bi and L. Wu, *Appl. Catal. B: Environ.*, 2015, **163**, 135-142.
49. S. Guo, Y. Tang, Y. Xie, C. Tian, Q. Feng, W. Zhou and B. Jiang, *Appl. Catal. B: Environ.*, 2017, **218**, 664-671.
50. J. Halim, K. M. Cook, M. Naguib, P. Eklund, Y. Gogotsi, J. Rosen and M. W. Barsoum, *Appl. Surf. Sci.*, 2016, **362**, 406-417.
51. P. Niu, L. Zhang, G. Liu and H.-M. Cheng, *Adv. Funct. Mater.*, 2012, **22**, 4763-4770.
52. Q. Han, B. Wang, J. Gao, Z. Cheng, Y. Zhao, Z. Zhang and L. Qu, *ACS Nano*, 2016, **10**, 2745-2751.
53. C. Shaowen, S. Baojia, T. Tong, F. Junwei and Y. Jiaguo, *Adv. Funct. Mater.*, 2018, **28**, 1800136.
54. R. Li, L. Zhang, L. Shi and P. Wang, *ACS Nano*, 2017, **11**, 3752-3759.
55. T. Su, H. Tian, Z. Qin and H. Ji, *Appl. Catal. B: Environ.*, 2017, **202**, 364-373.
56. Y. Huang, H. Xu, H. Yang, Y. Lin, H. Liu and Y. Tong, *ACS Sustain. Chem. Eng.*, 2018, **6**, 2751-2757.
57. P. Wu, J. Wang, J. Zhao, L. Guo and F. E. Osterloh, *J. Mater. Chem. A*, 2014, **2**, 20338-20344.
58. G. Dong, D. L. Jacobs, L. Zang and C. Wang, *Appl. Catal. B: Environ.*, 2017, **218**, 515-524.
59. J. S. Kim, J. W. Oh and S. I. Woo, *Catal. Today*, 2017, **293-294**, 8-14.
60. Y. Huang, K. Li, Y. Lin, Y. Tong and H. Liu, *ChemCatChem*, 2018, **10**, 1982-1987.
61. Z. Sun, M. Zhu, M. Fujitsuka, A. Wang, C. Shi and T. Majima, *ACS Appl. Mater. Interfaces*, 2017, **9**, 30583-30590.
62. X. Wang, K. Maeda, A. Thomas, K. Takanabe, G. Xin, J. M. Carlsson, K. Domen and M. Antonietti, *Nat. mater.*, 2009, **8**, 76-80.
63. L. Ge and C. Han, *Appl. Catal. B: Environ.*, 2012, **117-118**, 268-274.
64. M. A. Hope, A. C. Forse, K. J. Griffith, M. R. Lukatskaya, M. Ghidiu, Y. Gogotsi and C. P. Grey, *Phys. Chem. Chem. Phys.*, 2016, **18**, 5099-5102.
65. S. Chertopalov and V. N. Mochalin, *ACS Nano*, 2018, **12**, 6109-6116.
66. E. J. H. Lee, K. Balasubramanian, R. T. Weitz, M. Burghard and K. Kern, *Nat. Nanotechnol.*, 2008, **3**, 486.

67. R. Maiti, S. Haldar, D. Majumdar, A. Singha and S. K. Ray, *Nanotechnology*, 2017, **28**, 075707.
68. H.-J. Qiu, Y. Ito, W. Cong, Y. Tan, P. Liu, A. Hirata, T. Fujita, Z. Tang and M. Chen, *Angew. Chem. Int. Ed.*, 2015, **54**, 14031-14035.
69. I. Rahim, M. Shah, A. Khan, J. Luo, A. Zhong, M. Li, R. Ahmed, H. Li, Q. Wei and Y. Fu, *Sensor. Actuat. B-Chem.*, 2018, **267**, 42-50.
70. Y. Liu, J. Liu, Q. Ding, J. Tan, Z. Chen, J. Chen, X. Zuo, A. Tang and K. Zeng, *Macromol. Mater. Eng.*, 2018, **303**, 1800053.
71. M. Ghidiu, S. Kota, V. Drozd and M. W. Barsoum, *Sci. Adv.*, 2018, **4**, eaao6850.
72. M. Wang, M. Shen, L. Zhang, J. Tian, X. Jin, Y. Zhou and J. Shi, *Carbon*, 2017, **120**, 23-31.
73. R. Wang, L. Gu, J. Zhou, X. Liu, F. Teng, C. Li, Y. Shen and Y. Yuan, *Adv. Mater. Interfaces*, 2015, **2**, 1500037.
74. M. Yan, Y. Hua, F. Zhu, L. Sun, W. Gu and W. Shi, *Appl. Catal. B: Environ.*, 2017, **206**, 531-537.
75. S. I. Nikitenko, T. Chave, C. Cau, H.-P. Brau and V. Flaud, *ACS Catal.*, 2015, **5**, 4790-4795.
76. Z. Gan, X. Wu, M. Meng, X. Zhu, L. Yang and P. K. Chu, *ACS Nano*, 2014, **8**, 9304-9310.

Table of Contents

The separation of photogenerated carriers and photocatalytic hydrogen production efficiency was greatly enhanced by the 2D/2D heterojunction of Ti_3C_2/g-C_3N_4.